Japanese Journal of Applied Physics
Vol. 47, No. 2, 2008, pp. 964–968

Dynamic Structure and Mass Penetration of Shock Wave in Picosecond Laser-Material Interaction

Lijun ZHANG and Xinwei WANG*

Department of Mechanical Engineering, N104 Walter Scott Engineering Center, The University of Nebraska-Lincoln, Lincoln, NE 68588-0656, U.S.A.

(Received September 12, 2007; revised November 3, 2007; accepted November 25, 2007; published online February 15, 2008)

This work pioneers the atomistic modeling of the shock wave in background gas in picosecond laser-material interaction. It is found in the shock wave the compressed ambient gas region has a very uniform temperature distribution while the temperature decreases from the front of the plume to its end. The group velocity of atoms in the shock wave front is much smaller than the shock wave propagation speed and experiences a fast decay due to momentum exchange with the ambient gas. Strong decay of the shock wave front temperature and pressure is observed while its density features much slower attenuation. An effective mass penetration length is designed to quantitatively evaluate the mutual mass penetration between the plume and background gas. This effective mixing length grows at a rate of ~60 m/s. This fast mixing/mass penetration is largely due to the strong relative movement between the plume and the background gas. The molecular dynamics results agree well with the analytical solution in terms of relating various shock wave strengths. [DOI: 10.1143/JJAP.47.964]

KEYWORDS: shock wave, picosecond laser-material interaction, molecular dynamics simulation, dynamic structure, mass penetration

1. Introduction

Despite the wide spectrum of theoretical and experimental studies of laser-material interaction in material processing, the effect of background gas on the expansion dynamics of plume generated by laser ablation has not been well investigated. The interaction of laser ablation plume with a background gas rather than a vacuum in laser material processing has received increasing attention in recent years.[1,2] In laser-material interaction, the expansion of ablated molten nanoparticles will form a shock wave in a background gas, which could have profound impact on material processing. Moreover, the interaction of plume with ambient gas is a very complex gas dynamic process due to the occurrence of several involved physical processes, such as acceleration, deceleration, attenuation, thermalization, diffusion, and recombination of ablation species.[3] Laser-induced shock waves near the sample surface could cause fractionation during femtosecond to nanosecond laser ablation. Additionally, the induced recoil pressure and radiating heating of sample surface can significantly influence mass removal.[4] The amount of sample vaporized by the laser pulse,[5] the crater size,[6] pressure and density are found to be strongly influenced by the ambient atmosphere.[7] Voevodin *et al.*[8] studied the laser ablation deposition of yttria-stabilized zirconia (YSZ) films on the selection of background environment with low pressure oxygen and argon. Their work demonstrated that the background gas strongly affected plasma chemistry, excitation states and energetics during YSZ film growth. Harilal *et al.*[9–11] investigated the expansion dynamics of laser produced Al plasma at different ambient pressures. Zhang and Gogos[12] developed a theoretical model to describe the laser ablation in a background gas under the effects of laser intensity and background gas. Kapitan and Coutts[13] investigated the dynamic properties of shock waves generated during pulsed-laser ablation of solid aluminum targets at sub-atmospheric pressure by using the Sedov–Taylor–von Neumann theory. The general effect of the background gas is like a spatial confinement that slows down the plume expanding. Many experimental and theoretical works have been conducted on this effect. However, the underlying effects and mechanism of laser material interaction in the background gas are not satisfactorily explained. Furthermore, little knowledge is available about the internal dynamic structure and mass penetration of shock waves in laser-material interaction.

2. Basis of Molecular Dynamics Modeling

In this work, classical molecular dynamics (MD) simulation is conducted to explore the internal dynamic structure of shock waves in background gas under the consideration of non-reactive background ambient gas during fast pulsed laser ablation. This atomistic modeling is performed for a free-standing argon film (target) for generic physics study. The computational domain consists of 337,500 atoms, and measures $32.5 \times 3627 \times 2.7\,\mathrm{nm}^3$ ($x \times y \times z$). The solid target measures 108 nm in the y direction. In this direction, the background gas measures 271 nm below the target and 3248 nm above it. The model gas material is designed to have the same atomic mass as argon, but only have repulsive potential between gas-gas and gas-target atoms. This repulsive potential takes the same formula as that for argon. Such potential treatment for the model ambient gas significantly simplifies the computation without losing generality of the conclusion. Periodical boundary conditions are applied in the x and z directions. The optical field assumes a temporal Gaussian distribution with an energy fluence of $3\,\mathrm{J/m}^2$. The full width at half maximum (FWHM) of the laser pulse is 11.3 ps peaked at 9.5 ps. No specific laser wavelength is assumed in this work since the modeling is for generic physics study. The laser energy is absorbed exponentially in the target with an artificial optical absorption depth of 15 nm. This optical absorption depth is not intended to recover a specific wavelength laser beam absorption in a specific material, but rather merely to reflect the volumetric effect of laser absorption. Details of laser beam absorption and treatment of MD simulation can be found in our recent work about laser-assisted surface

*E-mail address: xwang3@iastate.edu

nanostructuring.[14] The half-step leap-frog scheme is used in this work with a time step of 25 fs. Computation of the force between an atom and its neighbors is arranged by the cell structure and linked-list method. The cutoff distance for MD simulation takes 2.5σ where σ is the equilibrium atomic separation in the Lennard-Jones potential. Before laser heating, equilibrium MD simulation is run for 100 ps with velocity scaling to make the system (target and ambient gas) reach 50 K. Then the system is calculated for another 100 ps to eliminate the small disturbance induced by velocity scaling. After equilibrium calculation, the pressure of the ambient gas is around 0.25 MPa. This value is very close to its pressure (0.27 MPa) calculated using the ideal gas equation. Therefore, in this work, the ambient gas is assumed ideal gas for the separate analytical analysis that will be compared with the MD result. Under this assumption, the sound speed in the ambient gas is calculated to be 132 m/s.

3. Results and Discussion

Figure 1 shows the snapshots of atomic positions in the x–y plane at different instants to illustrate the dynamic formation of the shock wave. Red dots are for the target argon material and blue dots represent the ambient gas. After 0.5 ns, the compressed ambient gas induced by laser ablation clearly shows a shock wave, which is the dark blue region in the figure. In laser-material interaction, the atoms in the near surface region explode out due to laser heating. Detailed research about laser ablation without an ambient gas has been reported before.[15–17] Since the laser fluence is strong enough to result in ablation, a plume is ejected from the target surface into the background gas. At this initial stage, the laser ablation does not have a big difference compared with the laser ablation in a vacuum. The reason is that at the initial stage of laser ablation, the plume mass and density are significantly larger than those of the adjacent background gas. The influence of the background gas is not so significant compared to plume expansion.

Nanoclusters are found to constitute a large part of the ejected plume near the surface region as shown in Fig. 1. However, when this high energy plume penetrates into the background gas continuously, accumulated mass of the ambient gas becomes comparable to that of the plume. Strong repulsion from the background gas prevents the ejected plume from expanding in space freely. This significantly reduces the velocity of the expansion plume and converts its kinetic energy into thermal energy. The thermodynamics properties of the ablation plume change dramatically. Clear contacts between the plume and shock wave (compressed ambient gas), and between the shock wave and ambient gas, can be seen in Fig. 1. The thickness of the shock wave grows during its propagation in space. The front of the shock wave has the highest density, and the density becomes smaller toward the plume-gas interface. The movement of the plume is significantly slowed down by the ambient gas. With the shock wave propagating in space, more ambient gas atoms are trapped in it. To further investigate the inside structure of the shock wave, the temperature and pressure distribution, as well mutual mass penetration between the plume and background gas are studied in detail.

Figure 2 shows the temperature distribution at three typical times: 0.5, 2, and 3 ns. Formation of the shock wave in background gas is induced by the fast movement of the plume, which acts like a piston to compress the ambient gas. The initial velocity of the plume should be higher than the sound speed of the ambient gas in order to induce a shock wave. Our study of the initial plume velocity shows that the plume front has a velocity over 400 m/s, much higher than the sound speed in the ambient gas (132 m/s). Based on the atomic positions shown in Fig. 1, the temperature distribution in Fig. 2 can be divided into five regions as indicated in

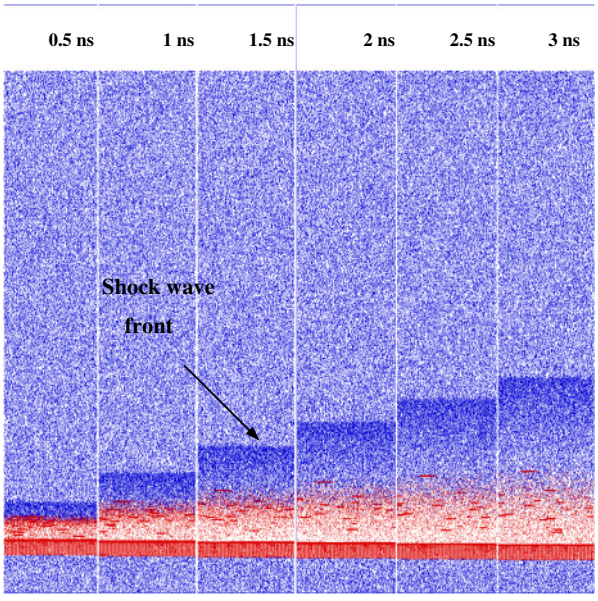

Fig. 1. (Color online) Dynamics of shock wave formation at different times in the x (horizontal: 0–32.5 nm)–y (vertical: 0–3627 nm) plane. Red dots: target material, blue dots: ambient gas. In order to plot the atoms in a more visible way, the aspect ratio of the figure is changed from that of the computational domain with the x coordinate expanded by a factor of 25.4.

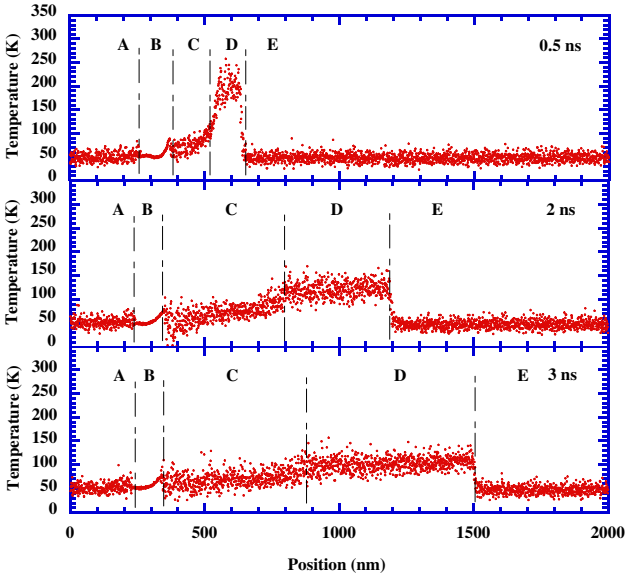

Fig. 2. (Color online) Temperature distribution in space at different times.

Fig. 2. Regions A and E are the normal ambient gas. Region B is the solid target material, region C the ablation plume, and region D the compressed ambient gas trapped in the shock wave. After the expanding plume spreads into the background gas, the high temperature and high pressure vapor creates a strong shock wave. The temperature rises sharply at the shock wave front due to shock wave compression. For the shock wave, its region C (ablation plume) has a temperature increasing from the target surface to the plume front. On the other hand, the region D (compressed ambient gas) has a very uniform temperature distribution. As the shock wave moves away from the target surface, more ambient gas atoms are trapped within the shock wave front, making the mass movement of the compressed gas slow down. Furthermore, the pressure drop behind the shock wave front also contributes to this deceleration. It is found the highest average mass/group velocity (different from the shock wave propagation velocity) appears in the front of the shock wave, and is about 360, 290, and 220 m/s at 0.5, 1, and 3 ns, respectively. Tracking the position of the shock wave front indicates that it propagates with a velocity from 468 m/s (0.5 ns) to 320 m/s (3 ns) in our simulation domain. It is evident that the mass/group velocity of atoms in the shock wave front falls behind the propagation of the shock wave front itself. This indicates the propagation of the shock wave is not a pure energy transfer process by the mass movement of atoms, but including a strong process of compressing the ambient gas and trapping them in the shock wave.

The Mach number (M_s) of the shock wave is related to the pressure ratio as $M_s^2 = 1 + (p_2/p_1 - 1)/(\gamma_1 + 1)/2\gamma_1$, where γ_1 ($= 5/3$) is the specific heat ratio of the ambient gas. Based on the pressure ratio, the range of Mach number is from 3.6 at 0.5 ns to 2.3 at 3 ns. The Mach number can also be directly calculated as $M_s = v_f/c$, where v_f is the shock wave front speed, and c is the sound speed in the background gas. Based on the shock wave front speed obtained above, the Mach number is calculated as 3.55 at 0.5 ns and 2.42 at 3 ns. These values agree well with the abovementioned analytical results. It is obvious that the trend of the Mach number also presents a decay during the shock wave propagation.

Figure 3 presents the pressure distribution at three typical times: 0.5, 2, and 3 ns. The average pressure is calculated as[14]

$$\sigma_{mm} = \frac{1}{\Delta V}\left(\sum_{i\neq j}^{N} r_{ij,m}F_{ij,m} + Nk_BT\right), \quad (1)$$

where ΔV is the volume of the domain of interest, and Nk_BT is the pressure induced by the movement of atoms. It is found that the pressures (P_{xx}, P_{yy}, P_{zz}) share the similar propagation style in the y direction. Therefore only the xx pressure is shown in Fig. 3. In order to give a clear view about the shock wave evolution, only the pressure of the ambient gas and the expansion plume is plotted. As mentioned before, the initial pressure of the ambient air is around 0.25 MPa. In the compressed gas domain (shock wave), the highest pressure at the shock wave front is in the order of 3.0, 2.0, and 1.5 MPa at 0.5, 2, and 3 ns respectively, which is much higher than the pressure of the ambient gas. The peak value of the pressure at the shock wave front shows a strong decay during the propagation.

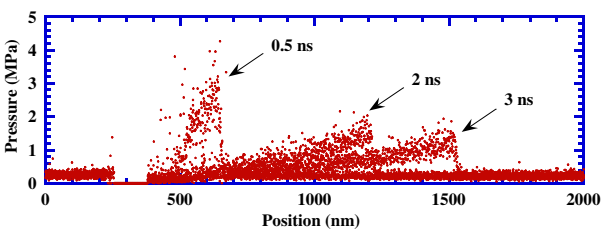

Fig. 3. (Color online) Pressure distribution in space at different times.

Besides the dynamic internal structure of the shock wave, one of the most interesting phenomena about shock waves in laser-material interaction is the mutual mass penetration between the ablation plume and ambient gas. This penetration phenomenon is very challenging to study in experiments due to its small existing region while it strongly affects the evolution of the ablation plume. Figure 4 shows the density distribution of the ablation plume and ambient gas to illustrate their mutual mass penetration. The density of the solid part is not our interest and is not shown in the figure. From 0.5 to 3 ns, it is observed that the co-existing region of the plume and ambient gas is becoming larger due to mutual mass penetration. During this period, the density of the ablation plume experiences a fast decay. The scattered big density values in the plume region come from the existence of nanoparticles/nanoclusters in the plume. The density distribution of the background gas shares the same trend as its pressure (P_b) distribution. This is understandable since the density (ρ_b) of the ambient gas is proportional to P_b/T_b, and the temperature T_b is almost constant in the shock wave region as indicated in Fig. 2. Figure 4 indicates that the co-existing region between the plume and background gas increases from about 100 nm at 0.5 ns to about 400 nm at 3 ns.

To obtain a better understanding of the mass penetration influenced by the background gas, a new parameter is introduced: effective mass penetration/co-existing length L_{mix}

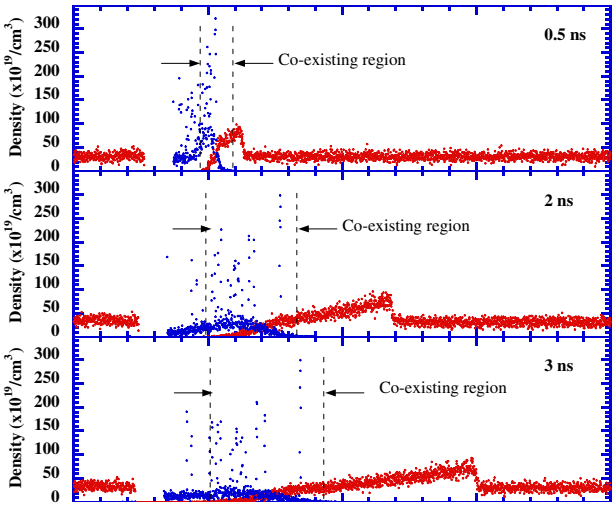

Fig. 4. (Color online) Density distribution in space at different times. Blue dots are for the ablated target material and red dots represent the ambient gas.

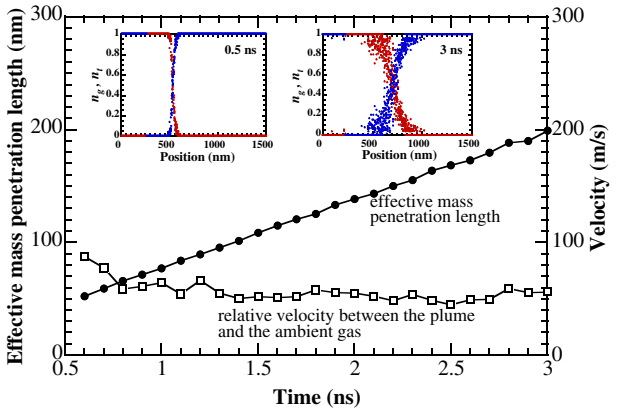

Fig. 5. (Color online) Evolution of the effective mass penetration length between the target and the ambient gas. The insets show the fraction distribution (n_g and n_t) of the target and gas at 0.5 and 3 ns (red dots: target material; blue dots: ambient gas).

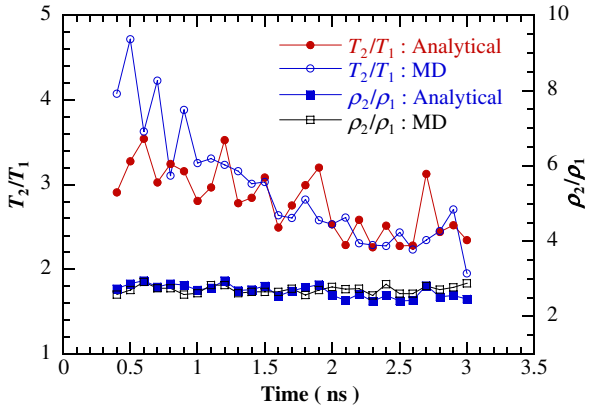

Fig. 6. (Color online) Decay of the temperature and density at the shock wave front.

$$L_{\mathrm{mix}} \equiv \int \frac{n_t n_g}{[(n_t + n_g)/2]^2}\, dx, \tag{2}$$

where $n_t = N_{\mathrm{target}}/(N_{\mathrm{target}} + N_{\mathrm{gas}})$ and $n_g = N_{\mathrm{gas}}/(N_{\mathrm{target}} + N_{\mathrm{gas}})$. Considering the fact $n_t + n_g = 1$, we have $L_{\mathrm{mix}} \equiv \int n_t n_g/4\, dx$. When calculating L_{mix}, the computational domain is divided into small layers of thickness Δx in the laser incidence direction. In this work, Δx takes the cut-off distance used in MD simulation. n_t and n_g represent the fraction of the target and gas atoms in the small layer. N_{target} and N_{gas} are the number of target and gas atoms in the small layer, respectively. In eq. (2), the value of L_{mix} will be non-zero only when both plume and gas co-exist in the area of interest.

Figure 5 shows the evolution of L_{mix} within a 3 ns time duration. Also shown in Fig. 5 (insets) are the fraction distribution (n_g and n_t) of the plume and gas at 0.5 and 3 ns. The effective mass penetration length changes from 44 nm at 0.5 ns to 200 nm at 3 ns, almost linearly with time. It is estimated that the effective mass penetration length grows at a rate of about 60 m/s. This mass penetration could be induced by two factors: pure mass diffusion between the plume and ambient gas (which is relatively slow), and the mass penetration by the strong relative movement between these two species. In order to address which factor mainly contributes to the mass penetration, the relative velocities/movement between the target and ambient gas are calculated. The relative velocity (in the laser incident direction) between the gas and plume is defined by the following form:

$$v_{\mathrm{rel}} \equiv \frac{\int |\bar{v}_{\mathrm{gas}} - \bar{v}_{\mathrm{target}}|\, dn}{N_{\mathrm{total}}}. \tag{3}$$

In eq. (3) $\bar{v}_{\mathrm{gas}}$ and $\bar{v}_{\mathrm{target}}$ are the ambient gas and ablated plume average velocities (in the laser incident direction) in each computational layer. N_{total} is the total number of gas and plume atoms within the co-existing area of ambient gas and plume. dn is the number of ambient gas and plume atoms in each computational layer. Only the region where the plume and ambient gas co-exit is considered. As shown in Fig. 5, the relative velocity is around 50–60 m/s, which is very close to the growing rate of the effective mass penetration length L_{mix}. This strongly proves that the main cause for the mutual mass penetration between the plume and the background gas is the strong relative movement between them.

To study the decay of the shock wave strength during its propagation, the ratio of temperature (T_2/T_1) and density (ρ_2/ρ_1) based on the MD data are calculated and shown in Fig. 6. The subscripts "1" and "2" denote the normal ambient gas and the shock wave front. According to analytical solutions,[18] the shock wave properties are related to the shock wave strength that is described by the ratio of the stagnation pressure and the ambient pressure expressed by the following forms:

$$\frac{T_2}{T_1} = \frac{P_2}{P_1} \times \left(\frac{(\gamma_1 + 1)/(\gamma_1 - 1) + P_2/P_1}{1 + (\gamma_1 + 1)/(\gamma_1 - 1) \times P_2/P_1} \right), \tag{4}$$

and

$$\frac{\rho_2}{\rho_1} = \frac{1 + (\gamma_1 + 1)/(\gamma_1 - 1) \times P_2/P_1}{(\gamma_1 + 1)/(\gamma_1 - 1) + P_2/P_1}. \tag{5}$$

Based on the P_2/P_1 calculated in this MD work, the temperature and density ratios are also calculated using eqs. (4) and (5) (denoted as "analytical" in Fig. 6). It is seen that the density of shock wave front has no appreciable decay within the time of calculation (3 ns) in this work, agreeing with the results shown in Fig. 4. Probably it will take a much longer time to decay. For the temperature of the shock wave front, it experiences a quick decay. Figure 6 shows that the MD simulation agrees well with the analytical solutions in terms of relating the pressure, density, and temperature ratios.

4. Conclusions

In summary, this paper reported the first time atomistic study of the shock wave formation in background gas, its dynamic structure, and mutual mass penetration in pico-second laser material interaction. It was observed that in the shock wave the compressed ambient gas region had a very uniform temperature distribution while the temperature decreased from the front of the plume to its tail. With the shock wave propagating in space, the atoms in the shock wave front moved at a relatively slow group velocity in comparison with the shock wave front propagation. Strong

decay of the shock wave front temperature and pressure was observed while its density featured much slower attenuation. An effective mixing length was designed to quantitatively evaluate the mutual mass penetration between the plume and background gas. This effective mixing length was observed to grow at a rate of about 60 m/s. The relative movement between the plume and the background gas had a significant contribution to this mass penetration. The MD results agreed well with the analytical solution in terms of predicting the relationship among various shock wave strengths.

Acknowledgement

Support for this work from NSF (CMS: 0457471), Nebraska Research Initiative, Air Force Office for Scientific Research and MURI from ONR is gratefully acknowledged. X. Wang also thanks the very helpful discussion with Dr. Zhaoyan Zhang at UNL.

1) D. B. Geohegan, A. A. Puretzky, G. Duscher, and S. J. Pennycook: Appl. Phys. Lett. **73** (1998) 438.
2) A. V. Bulgakov and N. M. Bulgakova: J. Phys. D **31** (1998) 693.
3) H. C. Le, D. E. Zeitoun, J. D. Parisse, M. Sentis, and W. Marine: Phys. Rev. E **62** (2000) 4152.
4) R. E. Russo, X. Mao, J. J. Gonzalez, and S. S. Mao: J. Anal. At. Spectrom. **17** (2002) 1072.
5) R. E. Russo, X. Mao, M. Caetano, and M. A. Shannon: Appl. Surf. Sci. **96** (1996) 144.
6) P. R. D. Mason and A. J. G. Mank: J. Anal. At. Spectrom. **16** (2001) 1381.
7) S. S. Harilal, C. V. Bindhu, V. P. N. Nampoori, and C. P. G. Vallabhan: Appl. Phys. Lett. **72** (1998) 167.
8) A. A. Voevodin, J. G. Jones, and J. S. Zabinski: J. Appl. Phys. **88** (2000) 1088.
9) S. S. Harilal, C. V. Bindhu, and H. J. Kunze: J. Appl. Phys. **89** (2001) 4737.
10) S. S. Harilal, C. V. Bindhu, V. Shevelko, and H. J. Kunze: J. Phys. B **34** (2001) 3717.
11) S. S. Harilal, R. C. Issac, C. V. Bindhu, V. P. N. Nampoori, and C. P. G. Vallabhan: J. Appl. Phys. **80** (1996) 3561.
12) Z. Y. Zhang and G. Gogos: Phys. Rev. B **69** (2004) 235403.
13) D. Kapitan and D. W. Coutts: Europhys. Lett. **57** (2002) 205.
14) X. Wang: J. Phys. D **38** (2005) 1805.
15) X. Wang and X. Xu: J. Heat Transfer **125** (2003) 1147.
16) X. Wang and X. Xu: Int. J. Heat Mass Transfer **46** (2003) 45.
17) X. Wang and X. Xu: J. Heat Transfer **124** (2002) 265.
18) J. D. Anderson: *Modern Compressible Flow with Historical Perspective* (McGraw-Hill, New York, 1982).